UWB Active Antenna for Microwave Breast Imaging Sensing Arrays

Farzad Foroutan and Natalia K. Nikolova, *Fellow, IEEE*

***Abstract*—An ultrawideband (UWB) active slot antenna for tissue sensing arrays is developed and measured to operate from 3 to 8 GHz. The sensing element reported here is to be used in the imaging of the breast. It integrates a low-noise amplifier (LNA) with a printed-slot antenna to achieve gain enhancement of about 20 dB. The first prototype integrates the biasing of the LNA on the same board as the antenna. The second prototype uses an external bias tee providing dc power to the LNA through the coaxial connector of the active antenna. Both prototypes achieve the expected gain enhancement in comparison with the passive antenna element.**

***Index Terms*—Active antenna, antenna array, active radio sensor, biased-switched array, microwave imaging, printed-slot antenna, ultrawideband (UWB).**

I. Introduction

THE concept of integrating radio-frequency (RF) active electronics within the antenna is well known, and examples can be found in scientific equipment [1], [2], microwave tissue imaging [3]–[5], medical radio-thermometers at 1.5 GHz [6], amplifier antenna arrays for spatial power combining [7], active antenna arrays with optical switching [8], ultrawideband (UWB) multiple-input–multiple-output (MIMO) systems [9], and other UWB applications [10], [11]. The p-i-n diodes have also been integrated with small metallic scatterers to control their resonant frequency [12]–[14].

The integration of a low-noise amplifier (LNA) with the antenna significantly improves the system signal-to-noise ratio (SNR), which is one of the greatest challenges in microwave tissue imaging. This is why the development of an active, i.e., LNA-integrated, antenna for tissue imaging arrays is critically important. In addition to the improved SNR, such antennas offer system size reduction since the LNA becomes part of the antenna element with no or very little increase in its size.

An active (10 dB gain) bow-tie antenna for medical microwave imaging has been proposed in [3] and [4]. The small size of this receiving antenna makes it suitable for array configurations. However, this design does not offer shielding from the back, which decreases the forward gain, increases the inter-element coupling, and makes the receiving array prone to the electromagnetic (EM) interference. In addition, the antennas are printed on a substrate with a relative permittivity of $\epsilon_r \approx 3.5$. This decreases the power coupled into high-permittivity tissues (e.g., muscle, brain, or radiologically dense breast), e.g., [15] reports tissue phantoms of permittivity $\epsilon_r \approx 33$.

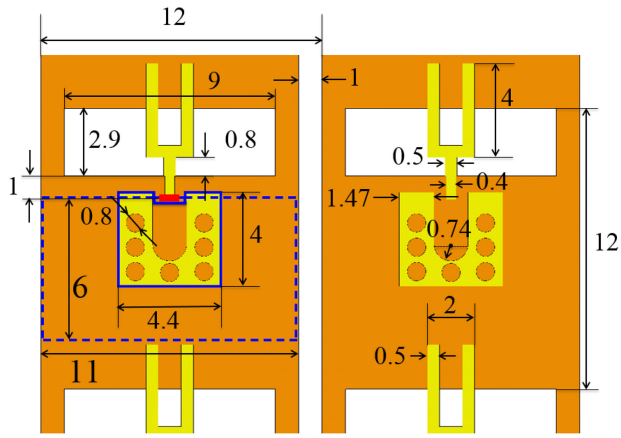

Fig. 1. Four neighboring antennas in the passive array reported in [16]. The ground pad of the coaxial connector (residing in the same metallization layer as the fork) is modeled in simulations by a continuous metallic sheet component (see blue solid outline) connected to the fork by an edge port (red rectangle). The area available for mounting an LNA circuit and a coaxial connector is about 11 mm × 6 mm (indicated by blue dashed line).

Here, we present the integration of the elements of a previously reported passive antenna array [16], [17] (see Fig. 1) with LNA chips on the same board. The array employs a slot-antenna element similar to that reported in [18], but thoroughly redesigned to achieve: 1) reduced equal spacing along x and y, and 2) shielding from the back. The latter is critical because it reduces interference, enhances the forward gain, and enables the integration of electronics at the back of the antenna printed circuit board (PCB). The array is printed on a Rogers substrate ($\epsilon_r = 10.2$) for maximum power transfer to breast tissues. Its passive structure has been investigated in detail in [16], where good impedance match is demonstrated in tissue measurements from 3 to 8 GHz. It is part of an active radio-sensor prototype, which consists of three separate PCBs: the antenna array, the LNA board, and the board of an active mixer. The sensor's output is at intermediate frequency and is to be used in large bias-switched arrays.

The current development demonstrates the successful integration of the first two modules of the radio sensor, namely, the antenna and the LNA chip [19], on a common PCB and without increasing the overall area occupied by the antenna itself. This

Manuscript received January 7, 2019; accepted July 12, 2019. Date of publication August 7, 2019; date of current version October 4, 2019. This work was supported in part by the Natural Sciences and Engineering Research Council of Canada (NSERC) under Grant RGPIN-2017-06058 and Grant EQPEQ-2015-472431. *(Corresponding author: Farzad Foroutan.)*

The authors are with the Department of Electrical and Computer Engineering, McMaster University, Hamilton, ON L8S 4L8, Canada (e-mail: foroutf@mcmaster.ca; nikolova@ieee.org).

Digital Object Identifier 10.1109/LAWP.2019.2929016

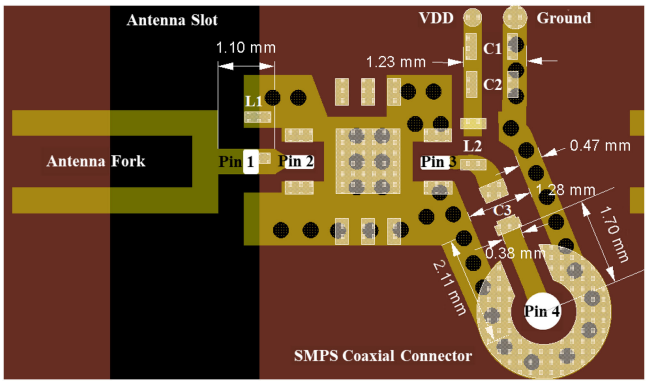

Fig. 2. Layout of the final design of the active antenna. In simulations of its S_{21} parameter, Pin 1 (end of the fork) is Port 1, whereas Pin 4 (output of the active antenna) is Port 2. Brown areas indicate the top layer facing the tissue, which contains the slots (black). Yellow areas indicate the bottom layer where the forks and electronics are. Beige areas indicate soldering pads for discrete components. DC bias of the LNA is provided through *VDD* and *Ground*. Circular via-holes (black) of diameter 0.3 mm connect the top and bottom layers. C1, C2, and C3 are chip capacitors. L1 and L2 are chip inductors.

active antenna is to be used in large-array configurations of several hundred radio sensors, in which the interelement spacing both in the x- and y-directions is 12 mm (the same as in the passive array reported in [16]). This development is critical not only for increasing the system SNR but also for the miniaturization of the sensor. It also eliminates the RF connectors between the antenna and the LNA, thus reducing cost and improving reliability and manufacturability.

In summary, the advantageous features of the proposed active antenna elements are: 1) 20 dB gain enhancement; 2) impedance bandwidth from 3 to 8 GHz; 3) small element size with center-to-center spacing of 12 mm; 4) easy-to-fabricate planar design; and 5) full shielding at the back. Yet, we note that the back shield negatively impacts the impedance match close to the 3 GHz end of the bandwidth.

II. Design and Simulation

The imaging array reported in [16] is an 11 × 11 passive printed-slot antenna array (see Fig. 1). The interelement center-to-center spacing is 12 mm × 12 mm. The array has two metallization layers on Rogers RT/Duroid 6010LM substrate with a dielectric constant 10.2 and thickness 0.635 mm. There is a slot at the top layer, which faces the tissue, and a fork at the bottom layer, which leads the received signal to a coaxial surface-mount connector. For the best match with measurements, the passive-array simulation (FEKO [20]) employs an edge port between the fork and the connector's ground pad, which is modeled as a continuous metallic sheet of shape tightly conforming to that of the actual pad (see Fig. 1). The array is shielded from the back with several dielectric layers leading to the metallic plane [16]. Fig. 1 shows that the connector occupies most of the area between a pair of elements that is available to mount an LNA. This necessitates major design changes so that this area accommodates both the LNA and the connector without compromising the impedance match.

The layout of the newly designed active antenna along with its dimensioning are shown in Fig. 2. It accommodates all the components of the original LNA evaluation board, including the bias tee. The footprint of the LNA chip and the values of the bias-tee components (chip capacitors and inductors) are those suggested in [19]. The antenna output (Pin 1) is connected to the input of the LNA (Pin 2). An inductor (L1) is mounted between the microstrip line at the end of the fork and the ground pad. The output of the LNA (Pin 3) connects to a surface-mount subminiature push-on submicro (SMPS) coaxial connector (Pin 4) through a 50 Ω finite-ground coplanar waveguide. Fig. 2 also shows the biasing chip capacitors (C1, C2, C3) and inductors (L1, L2).

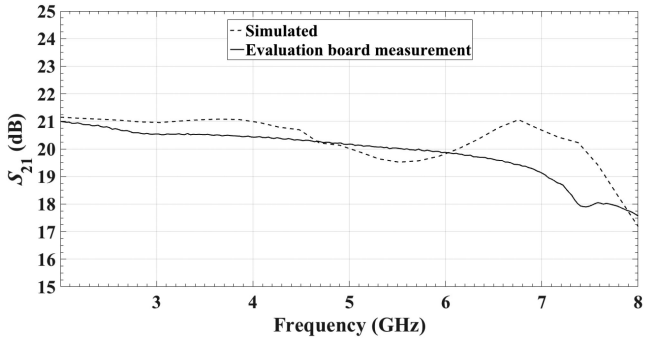

Fig. 3. Simulated gain of the designed circuit in Fig. 2 and the measured gain of the LNA evaluation board.

The S_{21} is simulated using Keysight Advanced Design System (ADS) co-simulation. Pin 1 (the end of the fork) is defined as Port 1. Pin 4 (output of the active antenna) is defined as Port 2. The S-parameters of the LNA chip are imported between Pin 2 (LNA input) and Pin 3 (LNA output) in the *schematic* part of the *co-simulation*. The simulated S_{21} is shown in Fig. 3, which also shows measured S_{21} of the LNA evaluation board for comparison. They match reasonably well, which demonstrates that the circuit's components are interconnected properly with good impedance match.

III. Measurements

A prototype array of 7 × 6 elements is fabricated. The array includes three different element types for comparison purposes. The first element type is shown in Fig. 2. It contains the antenna, the LNA chip, and its biasing circuit. The second and the third element types are shown in Fig 4. Fig. 4(a) shows the layout, which includes only the LNA chip, inductor L1, and the SMPS connector. This antenna uses an external bias tee providing dc power to the LNA through the SMPS connector. Fig. 4(b) shows a *passive* antenna, which includes only an SMPS connector. This element is added to make a comparison with the signal gains of the active antennas.

Fig. 5 shows photographs of the populated active and passive receiving antenna elements. Each element is surrounded by the remaining array elements (second type), which are not connected to a coaxial connector. This allows for element testing in a more realistic scenario where the neighboring elements affect its impedance match. Prior measurements on the passive array indicate that terminating the neighboring antennas with 50 Ω *short* or *open* loads has no influence on the impedance match of any given antenna element. This is due to the mutual coupling

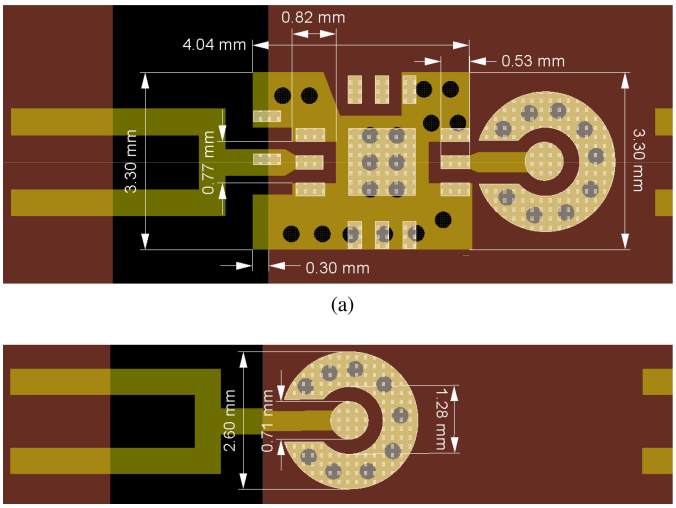

Fig. 4. (a) Second element type of an active antenna with the LNA chip and inductor L1 on board. The LNA bias is provided with an external bias tee through the SMPS connector. (b) Third element type of a passive antenna for comparison purposes.

between neighboring elements being less than -15 dB in the whole frequency band [21].

The fabricated antenna array includes backing layers partially visible in Fig. 6(b). Portions of these are cut out to allow access to the connectors. The thickness and permittivity values of the backing layers are as follows: The first layer (starting from the forks' layer) is a 0.635 mm thick Rogers laminate ($\epsilon_r = 10.2$), which in turn is backed with a 3.2 mm thick FR4 laminate ($\epsilon_r = 4.6$). This is then shielded with copper.

In order to evaluate the fabricated arrays, the received signals of all three element types are compared under identical measurement conditions, i.e., using the same transmitting antenna and tissue phantom. Port 1 of the Agilent Technologies E8363B PNA Network Analyzer is connected to the transmitting antenna (an in-house quad-ridge horn designed to transmit maximum power when in direct contact with phantoms of relative permittivity 10 [22]). Port 2 is connected to the receiving array element under test. The transmission coefficient S_{21} is measured with a flat-tissue phantom placed between the transmitting antenna and the receiving array, both of which are pressed against the sides of the phantom. The distance between the horn's aperture and the receiving slot equals the phantom's thickness, which is 4 cm. The breast-tissue phantom is homogeneous and made of carbon–rubber material [16] of real relative permittivity decreasing monotonically from 15 at 3 GHz to 10 at 8 GHz. Its imaginary part also decreases monotonically from 4 at 3 GHz to 2 at 8 GHz.

The measured S_{21} for the three types of elements is shown in Fig. 7. As expected, the signals received by the two active elements are amplified compared to the passive one. For both active elements, with on-board or external biasing, the differences are close to the LNA gain of about 20 dB.

The measured impedance match (S_{11}) of the third (passive) element is shown in Fig. 8. It is satisfactory in the desired bandwidth from 3 to 8 GHz. It is consistent with the simulations and the measurements of the passive antenna array element reported in [16]. The difference between simulation and measurement

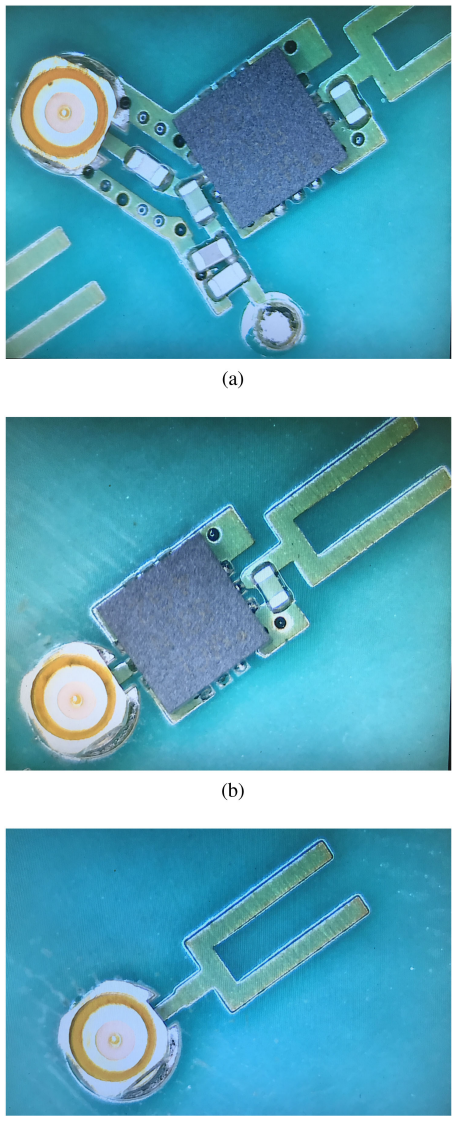

Fig. 5. Three fabricated element types. (a) First element type of an active antenna with the bias circuit on the same board. (b) Second element type of an active antenna with the LNA chip and inductor L1 only on the board. The LNA bias is provided with an external bias tee through the SMPS connector. (c) Third element type of a passive antenna for comparison.

is mostly due the simulations being based on a smaller array of 3×3 antennas (due to extensive computational demand), whereas the measured prototype consists of 11×11 antennas. The simulation employs a three-layer medium, where a 5 cm thick tissue layer resides between the two semi-infinite air layers. There is uncertainty in the phantom's electrical properties, which contributes to the discrepancy between simulation and measurement [16]. All three layers in the simulation are infinite in the lateral directions, whereas the actual phantom is finite (20 cm $\times$ 20 cm).

IV. Discussion

Radiation patterns are an important far-field antenna parameter. However, the receiving array reported here operates in direct contact with the tissue, capturing scattered signals emanating

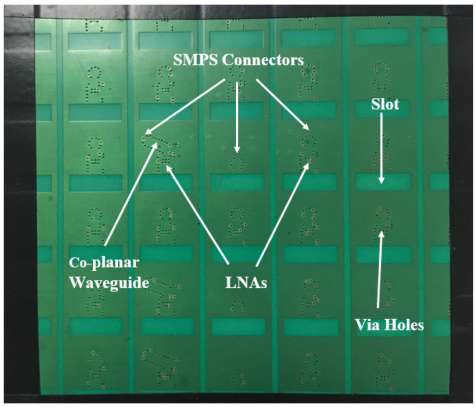

(a)

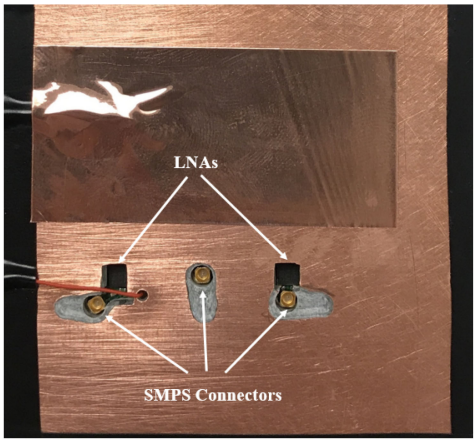

(b)

Fig. 6. Top and the bottom views of the fabricated antenna array with backing layers and shielding. (a) Top layer facing the tissue phantom. (b) Bottom shielding layer where the electronics and the connectors are.

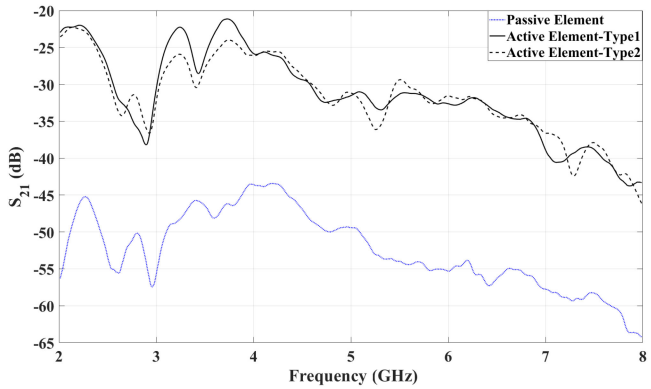

Fig. 7. Measured S_{21} for the elements shown in Fig. 5.

within its reactive near-field and Fresnel zones. Moreover, it does not operate in an open uniform medium, but rather in a layered medium (air–phantom–air). To appreciate the operating conditions, let us consider a tissue phantom of relative permittivity as stated in Section III. The wavelengths range from approximately 25.6 mm at 3 GHz to 11.8 mm at 8 GHz. At the same time, the breast-tissue phantom can have thicknesses ranging from 40 to about 70 mm [23], which places much of the imaged volume

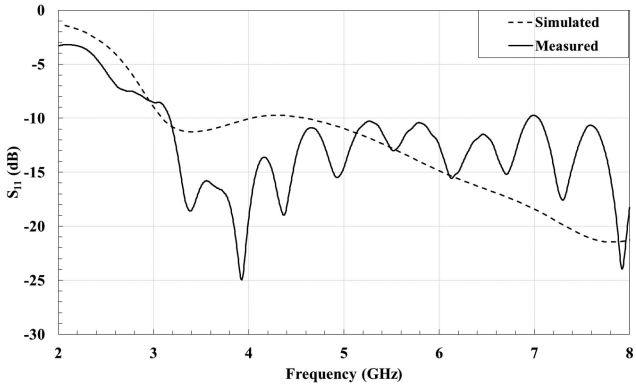

Fig. 8. Measured and simulated S_{11} of the passive antenna (third element type in the fabricated array) shown in Fig. 5(c).

within a wavelength or two from the slots. Note that the field behavior is also affected by neighboring elements. Even if the far-zone limits are estimated assuming a single array element (12 mm $\times$ 12 mm), they vary from 22.5 mm at 3 GHz to 48.8 mm at 8 GHz, which places almost the entire imaged volume outside the far-field zone. Therefore, the far-field patterns are not useful in this application. The near-field distributions could be of interest. They vary with frequency, distance to the array, and the field component. As an example, the near-zone distributions of the E-field magnitude are observed in simulations on a plane 36 mm $\times$ 36 mm (centered on the active slot's boresight) at a distance of 30 mm from the array. At 3 GHz, the distribution varies smoothly from 1.17 V/m at the edge to 2.07 V/m at the center. At 8 GHz, the variation remains smooth, with 80 mV/m at the edges and 480 mV/m at the center.

We briefly note that the mutual coupling of neighboring array elements (measured to be below -15 dB [21]) is of no concern in a bias-switched array [16]. The isolation of the receiving elements is near-perfect [24], [25] because, at each measurement, only the UWB receiver attached to the "activated" element is ON while those of all other elements are OFF. Finally, we note that reoptimizing the array for different tissue electrical properties must focus on substrate permittivity, slot size, array-element spacing, and position of the coaxial connector relative to the fork. The main performance parameter is the impedance match of the antenna element within a realistic (at least 3 $\times$ 3) array arrangement.

V. Conclusion

A UWB miniature active printed slot antenna is proposed and validated through measurements of two prototypes (with an on-board bias tee and with an external bias through the coaxial connector). A signal gain of about 20 dB is achieved in the frequency band from 3 to 8 GHz, which matches that of the LNA integrated on the antenna board. The two active element types exhibit comparable results.

Acknowledgment

The authors would like to thank T. Ackland and A. Pitcher for help with fabricating the prototypes.

REFERENCES

[1] M. A. Salari, O. Manoochehri, A. Darvazehban, and D. Erricolo, "An active 20-MHz to 2.5-GHz UWB receiver antenna system using a TEM horn," *IEEE Antennas Wireless Propag. Lett.*, vol. 16, pp. 2432–2435, 2017.

[2] A. A. Konovalenko, I. S. Falkovich, A. A. Gridin, P. L. Tokarsky, and S. N. Yerin, "UWB active antenna array for low frequency radio astronomy," in *Proc. 6th Int. Conf. Ultra-Wide Band Ultra-Short Impulse Signals*, Sep. 2012, pp. 39–43.

[3] M. Helbig *et al.*, "Experimental active antenna measurement setup for UWB breast cancer detection," in *Proc. IEEE Int. Conf. Ultra-Wide Band*, Sep. 2012, pp. 111–114.

[4] J. Sachs, M. Helbig, S. Ley, P. Rauschenbach, M. Kmec, and K. Schilling, "Short interfacial antennas for medical microwave imaging," in *Proc. Int. Workshop Antenna Technol.: Small Antennas, Innovative Structures, Appl.*, Mar. 2017, pp. 245–248.

[5] Y. L. Chow and S. Safavi-Naeini, "Active micropatch antenna device and array system," U.S. Patent 5 982 326, Nov. 9, 1999.

[6] S. Jacobsen and Ø. Klemetsen, "Improved detectability in medical microwave radio-thermometers as obtained by active antennas," *IEEE Trans. Biomed. Eng.*, vol. 55, no. 12, pp. 2778–2785, Dec. 2008.

[7] S. Pajic and Z. B. Popovic, "An efficient X-band 16-element spatial combiner of switched-mode power amplifiers," *IEEE Trans. Microw. Theory Techn.*, vol. 51, no. 7, pp. 1863–1870, Jul. 2003.

[8] J. Vian and Z. Popovic, "A transmit/receive active antenna with fast low-power optical switching," *IEEE Trans. Microw. Theory Techn.*, vol. 48, no. 12, pp. 2686–2691, Dec. 2000.

[9] A. K. Gautam, S. Yadav, and K. Rambabu, "Design of ultra-compact UWB antenna with band-notched characteristics for MIMO applications," *Microw., Antennas Propag.*, vol. 12, no. 12, pp. 1895–1900, 2018.

[10] M. Kumar, A. Basu, and S. K. Koul, "Active UWB antenna," in *Proc. URSI Int. Symp. Electromagn. Theory*, Aug. 2010, pp. 497–500.

[11] M. Jalali, A. Abdipour, A. Tavakoli, and G. Moradi, "An active integrated spiral antenna system for UWB applications," in *Proc. IEEE Int. Conf. Semicond. Electron.*, Oct. 2006, pp. 102–105.

[12] M. A. Abou-Khousa, M. T. Ghasr, S. Kharkovsky, D. Pommerenke, and R. Zoughi, "Modulated elliptical slot antenna for electric field mapping and microwave imaging," *IEEE Trans. Antennas Propag.*, vol. 59, no. 3, pp. 733–741, Mar. 2011.

[13] M. Ostadrahimi, M. Asefi, G. E. B. J. LoVetri, and L. Shafai, "An MST-based microwave tomography system using homodyne receiver," in *Proc. IEEE Int. Symp. Antennas Propag. Soc.*, Jul. 2013, pp. 814–815.

[14] D. A. Crocker and K. M. Donnell, "Application of electrically invisible antennas to the modulated scatterer technique," *IEEE Trans. Instrum. Meas.*, vol. 64, no. 12, pp. 3526–3535, Dec. 2015.

[15] M. Helbig, I. Hilger, M. Kmec, G. Rimkus, and J. Sachs, "Experimental phantom trials for UWB breast cancer detection," in *Proc. 7th German Microw. Conf.*, Mar. 2012, pp. 1–4.

[16] F. Foroutan and N. K. Nikolova, "Active sensor for microwave tissue imaging with bias-switched arrays," *MDPI Sensors*, vol. 18, no. 5, 2018.x

[17] F. Foroutan and N. K. Nikolova, "Dynamic range of an active radio sensor for bias-switched arrays for microwave tissue imaging," in *Proc. IEEE Int. Symp. Antennas Propag. USNC-URSI Radio Sci. Meeting*, Jul. 2018, pp. 11–12.

[18] T. Sugitani, S. Kubota, A. Toya, and T. Kikkawa, "A compact 4×4 planar UWB antenna array for 3-D breast cancer detection," in *Proc. IEEE Int. Symp. Antennas Propag. Soc.*, 2012, vol. 12, pp. 733–736.

[19] "TB-830A+ evaluation board." Accessed: Sep. 14, 2017. [Online]. Available: https://www.minicircuits.com/WebStore/dashboard.html?model=TB-830A%2B

[20] EM Software and Systems, S.A. (Pty) Ltd, FEKO Suite 7.0.1, Altair, Troy, MI, USA, 2017.

[21] F. Foroutan, "Active sensor for microwave tissue imaging with bias-switched arrays," Master's thesis, Dept. Elect. Comput. Eng., McMaster Univ., Hamilton, ON, Canada, 2018.

[22] S. Dadash, K. Moussakhani, and J. McCombe, "Quad-ridge horn antenna for tissue measurements," Computational Electromagnetics Res. Lab., McMaster Univ., Hamilton, ON, Canada, Tech. Rep. CEM-R-69, Jun. 2014.

[23] D. Tajik, F. Foroutan, D. Shumakov, A. Pitcher, and N. Nikolova, "Real-time microwave imaging of a compressed breast phantom with planar scanning," *IEEE J. Electromagn., RF, Microw. Med. Biol.*, vol. 2, no. 3, pp. 154–162, Sep. 2018.

[24] A. S. Beaverstone and N. K. Nikolova, "Switched sensor array for near-field microwave imaging of tissue," in *Proc. IEEE Int. Symp. Antennas Propag. USNC/URSI Nat. Radio Sci. Meeting*, 2015, pp. 354–355.

[25] A. S. Beaverstone and N. K. Nikolova, "Modeling and design of a switched transceiver array for tissue imaging," in *Proc. IEEE MTT-S Int. Conf. Numer. Electromagn. Multiphys. Model. Optim.*, Aug. 2015, pp. 1–3.